Available online at www.sciencedirect.com
ScienceDirect
Journal of the European Ceramic Society 31 (2011) 2671–2676
www.elsevier.com/locate/jeurceramsoc

Characterization and creep properties of proton-conducting Yb-doped barium cerate

C. Vaquero-Aguilar, M. Jiménez-Melendo *

Departamento de Física de la Materia Condensada, Universidad de Sevilla, Aptdo. 1065, 41080 Sevilla, Spain

Available online 26 January 2011

Abstract

Polycrystals of Yb-doped barium cerate with composition $BaCe_{0.95}Yb_{0.05}O_{3-\delta}$ have been synthesized via a solid-state reaction route. The ceramic has a single orthorhombic perovskite phase, and the crystallographic unit cell is almost unperturbed with respect to undoped $BaCeO_3$. The compound exhibits a homogeneous distribution of equiaxed and submicron grains. The high-temperature mechanical properties have been studied for the first time. Mechanical tests were carried out in compression between 1100 and 1250 °C in air at constant initial strain rate. A gradual brittle–ductile transition was observed with increasing temperature and/or decreasing strain rate. Grain boundary sliding is the main deformation mechanism in the ductile region. In this regime, the true stress–true strain curves display an unusual behavior, with an initial strength drop followed by an extensive steady-state stage. This behavior is accompanied by the emergence of new, fine grains along the boundaries and triple junctions of the original grains during deformation.

Keywords: D. Perovskites; A. Sintering; B. Microstructure-final; C. Creep; Cerate

1. Introduction

In the last few years, perovskite-structured oxides of generic formula ABO_3, where A^{2+} and B^{4+} denote site cations (for example, $BaCeO_3$, $SrCeO_3$ and $SrZrO_3$) are receiving increasing attention because of their remarkable proton conducting performance at intermediate temperatures.[1–5] This property is of prime importance for practical applications in the field of electrochemical energetics, particularly as electrolytes in solid oxide fuel cells (SOFCs). These devices can electrochemically convert hydrocarbons with high efficiency and low emissions. Substitution of B^{4+}-site by trivalent ions in these perovskite oxides causes the formation of oxygen vacancies, which allow for protonic conduction (hydrogen ion transport) upon exposure to water vapor at relatively high temperatures. Due to the higher mobility of protons compared to oxygen ions, the operating temperature of SOFCs can be safely reduced without lowering performance. Such a device could compete with conventional energy conversion devices if the requirements of long-term durability and reliability are met.

Trivalent cations such as Y^{3+}, Yb^{3+}, Nd^{3+} and Gd^{3+}-doped barium cerates are a prototype of this class of proton conducting oxides. They exhibit one of the highest proton and ionic conductivities at elevated temperatures, as well as an excellent chemical stability over a large range of temperatures and oxygen partial pressures.[4–6] Most of the investigations on doped-barium cerates are concerned with their processing, structure, defect chemistry and conductivity characteristics. Very few studies, in contrast, have focused on the high-temperature mechanical properties of these solid-state proton conductors.[7–9] These properties are, however, of special relevance in the design of SOFCs and other high-temperature operating devices because at the working conditions, deformation, mechanical degradation and failure determine the material behavior and ultimate overall performance. In addition, high-temperature plastic deformation is usually controlled by diffusion, and can thus provide basic information about mass transport in the compounds. Since sintering and grain growth are governed by diffusional processes, such information can be used to devise optimum processing schedules.

Furthermore, it has been usually assumed that the trivalent dopants exclusively occupy the Ce^{4+}-site, which introduces oxygen vacancies into the perovskite structure and furthers the protonic conductivity. Recent studies, [10–12] however, indicate

* Corresponding author. Tel.: +34 954550938; fax: +34 954552870.
E-mail address: melendo@us.es (M. Jiménez-Melendo).

0955-2219/$ – see front matter © 2011 Elsevier Ltd. All rights reserved.
doi:10.1016/j.jeurceramsoc.2011.01.001

that dopant partitioning can occur, such that a non-negligible concentration of trivalent ions resides onto the Ba^{2+}-site; this site transfer consumes oxygen vacancies, which is unfavorable for the ulterior water/proton uptake. These studies also showed that partitioning is restricted for small ionic radii dopants (compared to Ce^{4+}). In this sense, Yb^{3+} has essentially the same ionic radius than Ce^{4+} (0.87 Å[13]), and is therefore expected to lead to the ideal (maximum) oxygen vacancy content available for proton conductivity. To our knowledge, there are no studies on the microstructural characterization of ytterbium-doped barium cerate ceramics and their high-temperature mechanical properties. Therefore, the objective of this work was twofold: to synthesize Yb-doped $BaCeO_3$ with perovskite structure by solid state reaction and characterize the crystallographic structure and microstructure, and to investigate its mechanical behavior at elevated temperatures by means of compressive creep tests at constant initial strain rate in order to assess the strength of the material.

2. Experimental procedure

2.1. Sample preparation

Polycrystalline $BaCe_{0.95}Yb_{0.05}O_{3-\delta}$ (BC5Yb) was produced via a solid-state reaction route. Commercial powders of $BaCO_3$, CeO_2 and Yb_2O_3 (Aldrich, purity > 99.0%) were weighted in the required stoichiometric ratio, mixed and ground in agate media for 1 h using a planetary ball mill. The resulting powder was calcined for 10 h at 1200 °C in air and then carefully reground. At this point, the crystal structure of the powder was checked by X-ray diffraction (see below), which confirmed the presence of a single orthorhombic perovskite phase. Green pellets were obtained by uniaxial pressing at 150 MPa and isostatic pressing at 210 MPa. A two-step sintering process was performed on the pellets in air atmosphere at low heating and cooling rates: a first step at 600 °C for 2 h to eliminate water and hydroxides formed during intermediate stages, and a second sintering step at 1550 °C for 10 h. The final density of the samples, determined using Archimedes' method, was about 90–95% of the theoretical value of barium cerate (6360 kg/m^3). Osman et al.[6] reported a density of 91% in $BaCe_{0.95}Yb_{0.05}O_{3-\delta}$ prepared via a sol-gel method and sintered at 1500 °C for 10 h; the final grain size was not reported.

2.2. Crystal structure determination

The structural analysis of the crystalline phases in the calcined powders and sintered pellets was performed on X-ray powder diffractograms obtained using a Bruker AXS D8 Advance X-ray diffractometer in Bragg-Bentano configuration with Cu Kα radiation (X-ray Laboratory, CITIUS, University of Sevilla, Spain). A continuous scan mode was used to collect 2θ data from 10° to 120° in steps of 0.02° and a counting time of 10 s/step. X-ray tube voltage and current were set at 40 kV and 30 mA, respectively. Collected X-ray spectra were processed by the Le Bail refinement method using the TOPAS 4.2 Bruker AXS software package.

2.3. Mechanical tests and microstructural studies

Specimens of 5 mm × 3 mm × 3 mm in size were cut from the sintered pellets with a low-speed diamond saw and used for mechanical testing. Compression tests were carried out at temperatures T between 1100 and 1250 °C ($0.74T_m < T < 0.82T_m$, where $T_m = 1850$ K is the melting temperature of $BaCeO_3$) at constant cross-head speed. Experiments were performed in air atmosphere because Park et al.[7] found that the high-temperature deformation of $BaCe_{1-x}Y_xO_{3-\delta}$ ($x = 0.05$–0.20) was independent of testing atmosphere. The specimens were sandwiched between CSi pads in order to reduce the friction with the alumina push rods of the deformation machine, which tends to cause plastic constrictions at the ends of the specimen. The recorded data, load vs. time, were plotted as $\sigma - \varepsilon$ curves, where ε is the true strain ($\varepsilon = \ln(l_o/l)$, with l_o and l the initial and instantaneous length, respectively) and σ is the true stress ($\sigma = \sigma_o \exp(-\varepsilon)$, with σ_o the initial stress). Samples were typically deformed to total strains of 50%. At test completion, the specimen height was measured and compared with the value expected from the cross-head speed applied during the test; differences smaller than 1% were found in all cases. On the other hand, the previous equation for true stress is valid for homogeneous deformation at constant volume. This assumption has been proven to be valid for specimens deformed in the ductile region (see below). The data were analyzed using the standard high-temperature power law for steady-state deformation:

$$\dot{\varepsilon} = A\sigma^n d^{-p} \exp\left(\frac{-Q}{RT}\right) \quad (1)$$

where A is a parameter depending on the deformation mechanism, d is the grain size, n is the stress exponent, p is the grain size exponent, Q is the activation energy for flow and R is the gas constant.

The microstructural characterization of as-fabricated and deformed polycrystals was carried out using conventional (SEM) and high-resolution (HRSEM) scanning electron microscopy (Microscopy Service, CITIUS, University of Sevilla, Spain). To reveal grain boundaries, longitudinal sections were cut from the samples and mechanically polished using up to 1 μm grade diamond paste, and then thermally etched at 1200 °C for 2 h in air. The relevant morphological parameters, grain size d (taken as the equivalent planar diameter $d = (4(\text{grain area})/\pi)^{1/2}$) and form factor F (defined as $F = 4\pi(\text{grain area})/(\text{grain perimeter})^2$) were measured by using a semiautomatic image analyzer. Fracture surfaces of samples that either failed during testing or were intentionally broken at room temperature were also characterized by HRSEM.

3. Results and discussion

The calcined powder as well as the sintered pellets were identified by X-ray diffraction as being pure orthorhombic perovskite phase, with space group *Pmcn*. Fig. 1 shows the X-ray diffractogram of the sintered BC5Yb ceramic; the peak positions correspond to the orthorhombic structure of undoped $BaCeO_3$ (ICSD pattern No. 01-082-2425[14]). The lattice param-

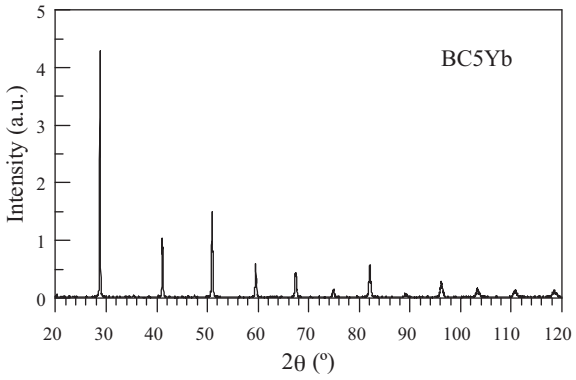

Fig. 1. X-ray diffraction pattern of sintered $BaCe_{0.95}Yb_{0.05}O_{3-\delta}$ polycrystal.

eters calculated using the Le Bail refinement method are given in Table 1, along with relevant literature data for barium cerate perovskites[14–16]; effective ionic radii of dopant ions[13] are also shown. It can be seen that the crystallographic unit cell of undoped $BaCeO_3$ is barely perturbed by the Yb-doping. Assuming in a first approach that the oxidation states of Yb and Ce are not modified by the oxygen nonstoichiometry, this result suggests that the dopant ions have fully occupied the Ce^{4+}-site, and not the Ba^{2+}-site, owing to the almost identical ionic radii of Yb^{3+} and Ce^{4+}. A cell volume contraction would be expected otherwise, due to the large difference in ionic radii between Yb^{3+} and Ba^{2+} cations. This result is especially relevant for the protonic conduction of the compound, since incorporation onto the Ce^{4+}-site is accompanied by the generation of oxygen vacancies, which in turn assist for proton uptake. Wu et al.[5,11] also concluded, from a variety of techniques including X-ray powder diffraction, electron microprobe chemical analysis and extended X-ray absorption fine structure spectroscopy (EXAFS), that little ytterbium, if any, was incorporated onto the A-site in $BaCe_{0.85}Yb_{0.15}O_{3-\delta}$.

Moreover, if the trivalent dopant ions were incorporated exclusively onto the cerium site, the perovskite cell volume should increase monotonically with increasing dopant ionic radius R. Data collected in Table 1, however, do not show this trend; in fact, Pr-doped $BaCeO_3$ exhibits the smallest cell volume despite having the largest ionic radius. This result can be explained if, due to size mismatch, the incorporation onto the Ba^{2+}-site is more favorable for the larger cations. This trend agrees with previous results[5,10,11] which show that dopant transfer from the Ce^{4+}- to the Ba^{2+}-site becomes more favorable as the dopant ionic radius increase.

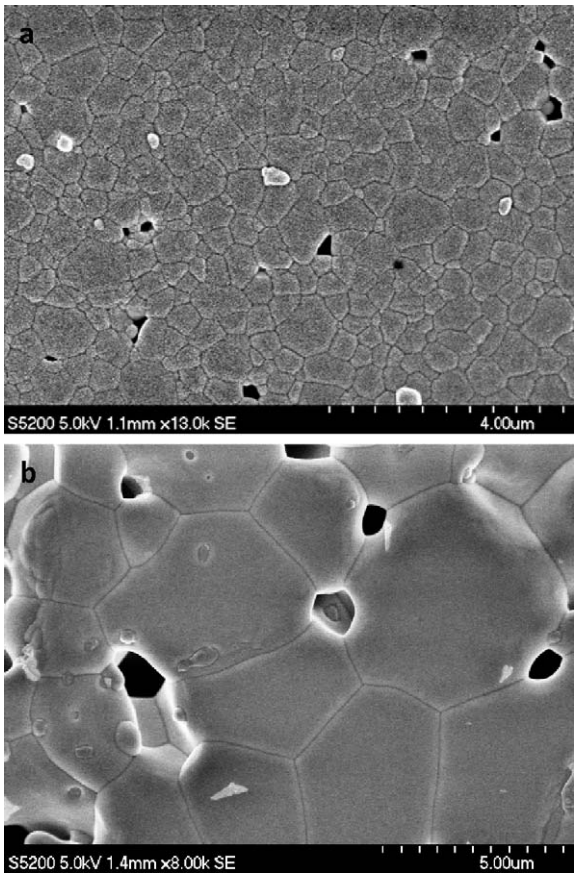

Fig. 2. SEM micrographs of polished and thermally etched cross-sections of polycrystalline: (a) $BaCe_{0.95}Yb_{0.05}O_{3-\delta}$ and (b) undoped $BaCeO_3$.

Fig. 2(a) shows a typical SEM micrograph of a polished and thermally etched cross-section of the as-fabricated polycrystal. The microstructure is very fine and homogeneous, formed by equiaxed grains with an average form factor $F = 0.75$. Porosity is exclusively intergranular, with small pores of size less than 1 μm. The grain size distribution is consistent with a lognormal law (Fig. 3(a)), as found in other ceramics.[17] The two characteristic parameters of this type of distribution, the mean grain size, d, and the standard deviation of $\ln d$, σ_d, can be easily deduced from the plot on a log probability paper of the cumulative percentage frequency against the logarithm of the grain size (Henry's plot, Fig. 3(b)). An average grain size d of 0.38 μm and a standard deviation of $\ln d$ of 0.49 were estimated from this plot. Almost the same grain size and shape were found in barium cerate doped with the same amount of yttrium, processed by a similar route.[9]

Table 1
Comparison of lattice constants and unit cell volumes for barium cerate perovskites $BaCe_{1-x}M_xO_{3-\delta}$ ($\delta = x/2$). Estimated errors in the last digits are given in parentheses. Ionic radii R of dopant ions[13] are shown. R (Ba^{2+}) = 1.35 Å, R (Ce^{4+}) = 0.87 Å.

Material	R (Å)	a (Å)	b (Å)	c (Å)	V (Å^3)
$x = 0$ (ICSD No. 01-082-2425)[14]		8.77362	6.23425	6.21346	339.86
M = Yb, $x = 0.05$ (this work)	0.87	8.77719 (72)	6.21327 (55)	6.23058 (54)	339.79
M = Y, $x = 0.10$[15]	0.90	8.7704	6.2386	6.2232	340.50
M = Gd, $x = 0.10$[15]	0.94	8.7732	6.2447	6.2216	340.86
M = Nd, $x = 0.08$[16]	0.98	8.78415	6.23369	6.22016	340.60
M = Pr, $x = 0.15$[14]	0.99	8.76954	6.23023	6.21005	339.41

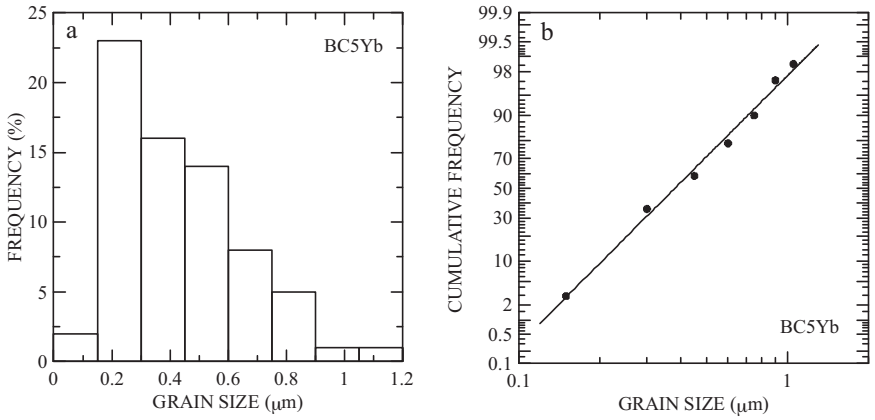

Fig. 3. Grain size distribution of the as-sintered Yb-doped barium cerate: (a) frequency histogram of d; (b) plot on log probability paper of the cumulative grain size frequency vs. log d.

For the sake of comparison, undoped barium cerate was also fabricated by the same procedure. The compound shows a duplex microstructure (Fig. 2(b)), formed by large, equiaxed and well-faceted grains of about 4 μm in diameter and small grains of about 0.5 μm in diameter located along the grain boundaries and inside the large grains. This results indicates that ytterbium doping dramatically increases the resistance to grain coarsening at elevated temperatures of the perovskite, as found in other ceramics.[18,19]

Regarding the mechanical properties at high temperatures, different behaviors were observed depending on temperature T and initial strain rate $\dot{\varepsilon}_o$. Fig. 4 shows typical true stress σ–true strain ε curves obtained at 1150, 1200 and 1250 °C and various deformation rates. For the lower T and higher $\dot{\varepsilon}_o$, the compound failed catastrophically after relatively small strains. This behavior disappears gradually when the strain rate decreases and/or the temperature increases, until large strains were achieved without any signal of damage. The macroscopic aspect of the strained samples (Fig. 5) correlates well with the corresponding stress–strain curves. At the lower $\dot{\varepsilon}_o$ and higher T, the specimens underwent a rather homogeneous deformation without any appreciable barreling (ductile region). As T decreased and/or $\dot{\varepsilon}_o$ increased, macroscopic cracks parallel to the loading direction developed on the lateral surfaces (semibrittle region). These cracks developed faster at highest strain rates and lowest temperatures, fracturing the sample into small pieces (brittle region).

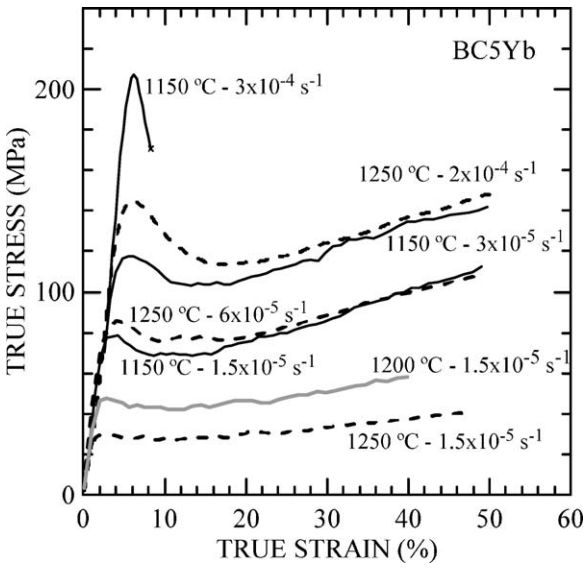

Fig. 4. True stress against true strain curves for $BaCe_{0.95}Yb_{0.05}O_{3-\delta}$ deformed at 1150 (black solid line), 1200 (grey solid line) and 1250 °C (black dashed line) and at different initial strain rates.

In the ductile region, the σ–ε curves exhibit an unusual behavior when compared to other fine-grained ceramics. There is systematically a peak stress at the beginning of the deformation, followed by a controlled stress drop and then by an extensive secondary creep regime (Fig. 4). This steady-state regime is characterized by a positive slope in a σ–ε plot due to sample shortening during a compressive constant cross-head speed test, which monotonically increases the instantaneous strain rate with respect to $\dot{\varepsilon}_o$. The magnitude of the stress drop (the difference between upper and lower yield stresses) decreases when decreasing the strain rate or increasing the temperature. Furthermore, the critical strain at which the peak stress appears shifts slightly to lower strains with increasing T or decreasing $\dot{\varepsilon}_o$ (Fig. 4).

The mechanical characteristics exhibited by the BC5Yb polycrystals in the ductile region are very similar to those reported recently for barium cerate doped with the same amount of yttrium, $BaCe_{0.95}Y_{0.05}O_{3-\delta}$.[9] Reports about the presence of initial stress drops followed by extensive steady-state flow are very scarce in ceramic polycrystals. Morita et al.[20] reported yield drops in a fine-grained ($d < 1$ μm) tetragonal ZrO_2–30 vol% spinel composite, which was attributed to a sudden increase in the mobile dislocation density within the spinel grains. In large-grained ($d > 5$ μm) MgO[21] and TiC,[22] yield drop was also ascribed to dislocation multiplication inside the grains. These dislocation-based mechanisms, similar to that found in single crystals with low initial dislocation density, usually result in rather sharp stress drops, which are little affected by strain rate. On the contrary, many studies in metals and metallic alloys at hot deformation conditions have reported a mechanical behavior similar to that found in the present study, where the yield stress depends on strain rate and temperature.[23–26] In these materials, the peak stress, the softening stage and the subsequent steady-

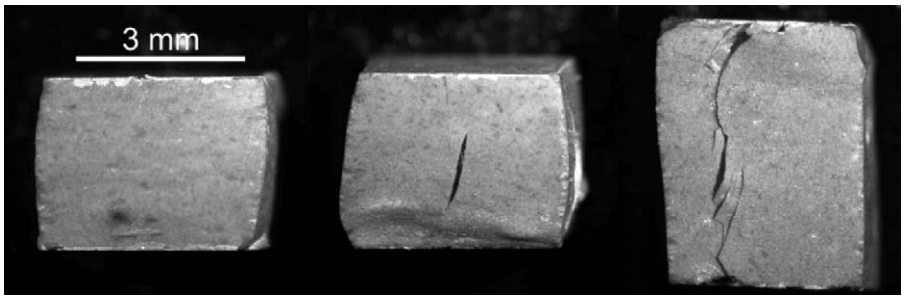

Fig. 5. Macroscopic aspect of strained samples. From left to right: ductile ($\varepsilon = 50\%$), semibrittle ($\varepsilon = 50\%$) and brittle ($\varepsilon = 10\%$) deformation.

state flow result from a dynamic balance between dislocation work hardening, dynamic recovery and dynamic recrystallization, leading to a refinement of the average grain size.

Microstructural observations of samples deformed in the ductile regime showed a distinct feature with respect to the unstrained analogs: the presence of new, fine grains along the boundaries and triple junctions of the original grains (Fig. 6, compare with Fig. 2(a)). The original grains maintained their average grain size d and form factor F essentially unaffected by the deformation process. Since the grains were not deformed even to strains up to more than 50%, they had to slide on each other to accommodate the macroscopic deformation of the specimen. Grain boundary sliding (GBS) is, therefore, the primary deformation mechanism at such experimental conditions, as usually found in fine-grained superplastic metals and ceramics.[19,27] As T decreases or $\dot{\varepsilon}_o$ increases, GBS is not fast enough to accommodate the deformation rate imposed, and cracks develop along grain boundaries leading eventually to macroscopic failure.

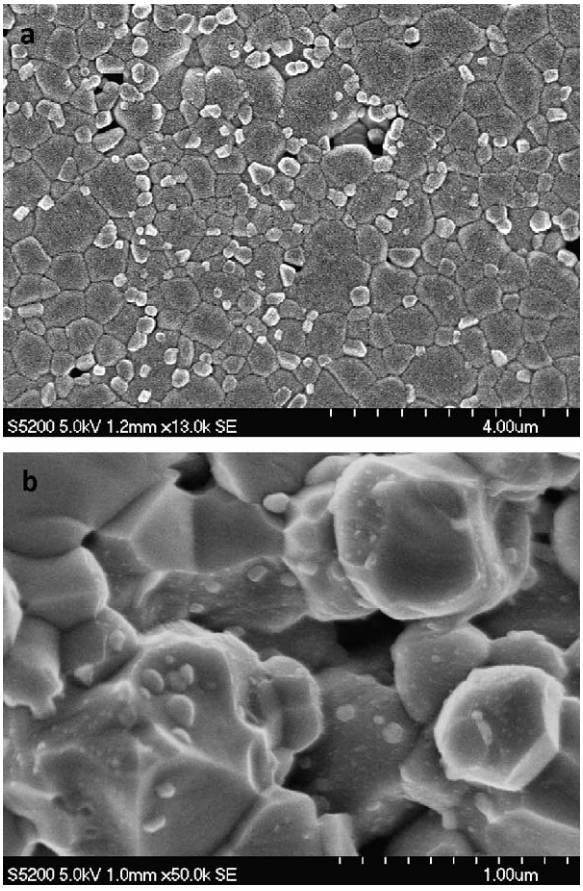

Fig. 6. SEM micrographs of 50%-strained $BaCe_{0.95}Yb_{0.05}O_{3-\delta}$ ($T = 1250\,^{\circ}C$, $\dot{\varepsilon}_o = 2 \times 10^{-5}\,s^{-1}$): (a) polished and thermally etched cross-section (stress axis is vertical) and (b) fracture surface obtained by intentionally breaking the sample after test.

As noted above, the mechanical characteristics exhibited by the true stress–true strain curves (Fig. 4) are very similar to those reported for metals with low to medium stacking fault energy.[23–26] In these materials, work hardening and dynamic recovery initially control the flow stress. When the strain exceeds a critical value, new grains nucleate and new high-angle boundaries grow, the driving force being the removal of dislocations. This softening mechanism leads to a peak in stress, which decreases until a steady-state flow is attained. The particular values of the critical strain, peak stress and flow stress level depend strongly on microstructural and testing parameters: temperature, strain rate, initial grain size, etc. In the present work, the emergence of new, fine grains during the high-temperature plastic deformation of the perovskite also results in an overall decrease of the average grain size. As a consequence, for a given strain rate, the flow stress will decrease (according to the inverse dependence of the strain rate with grain size (Eq. (1)) after reaching the critical strain required to trigger recrystallization.

A tentative stress exponent n (Eq. (1)) of 1.7 has been deduced from the fit of $\dot{\varepsilon}_o - \sigma$ data, measured in the steady-state regime. This value strengthens the previous conclusion derived from microstructural observations that GBS is the main deformation mechanism in the ductile region because it compares well with the value of 2 predicted by most theoretical models developed to explain superplasticity.[27] Additionally, when deformation is achieved by GBS, diffusion is usually the rate-controlling mechanism.[27] The activation energy for creep (Eq. (1)) can be thus identified with the diffusion energy of the slowest moving species in the compound. In this work, an apparent activation energy of $Q = 350$ kJ/mol was determined from the fit of $\sigma - 1/T$ data at given initial strain rates. However, the lack of enough diffusion data for doped barium cerates prevents a precise determination of the rate-controlling species. Only the activation energy for oxygen bulk diffusion $Q \approx 60$–100 kJ/mol has been reported.[7,28] The large difference with the present value suggests that diffusion of either Ba or Ce is the rate-limiting process. The same conclusion was drawn by Park et al.[7] in the study of yttrium-doped barium cerate with different amounts of doping. In this regard, the n and Q values measured in the present work

are very similar to those reported for $BaCe_{0.95}Y_{0.05}O_{3-\delta}$,[9] indicating that the same deformation mechanisms control the plastic behavior of doped barium cerates.

4. Conclusions

Ytterbium-doped barium cerate polycrystals with composition $BaCe_{0.95}Yb_{0.05}O_{3-\delta}$ has been successfully fabricated by solid state reaction. The resulting compound exhibits a single orthorhombic perovskite phase, with space group *Pmcn*. The measured lattice parameters indicate that the crystal structure of the undoped material remains essentially unaffected by doping. Based on the similarity between the ionic radii of Yb^{3+} and Ce^{4+}, this result suggests that dopant ions were incorporated almost exclusively onto the Ce^{4+}-site, ensuring the ideal (maximum) oxygen vacancy content for ulterior proton uptake. The microstructure consists of fine and equiaxed grains of about 0.4 μm in size, with small intergranular pores. Compressive tests were performed at constant cross-head speed in air at temperatures of up to 1250 °C. A gradual brittle–ductile transition occurs when the temperature increases and/or the strain rate decreases. In the ductile region, deformation is achieved mainly by grain boundary sliding. The corresponding true stress–true strain curves display an unusual behavior, with an initial strength drop followed by an extensive steady-state regime. The magnitude and position of the peak stress depends on temperature and strain rate. These features are characteristic of hot-deformed metals and alloys, where dynamic recrystallization takes place. In the present material, new fine grains emerge along the boundaries and triple junctions of the original grains during deformation. The overall average grain size is thus refined, explaining the occurrence of stress drops. When the strain rate increases and the temperature decreases, sliding is not longer accommodated and cracking takes place without plastic deformation of the grains.

Acknowledgment

This work was supported by the Project no. MAT2009-13979-C03-01, Ministerio de Ciencia e Innovación, Spain.

References

1. Kreuer KD. On the development of proton conducting materials for technological applications. *Solid State Ionics* 1997;**97**(1–4):1–15.
2. Guan J, Dorris SE, Balachandran U, Liu M. Transport properties of $BaCe_{0.95}Y_{0.05}O_{3-\alpha}$ mixed conductors for hydrogen separation. *Solid State Ionics* 1997;**100**(1–2):45–52.
3. Ito N. Intermediate-temperature SOFCs using proton-conducting perovskite. Perovskite oxide for solid oxide fuel cells. In: Ishihara T, editor. *Fuel cells and hydrogen energy series*. Springer; 2009.
4. Maekawa H, Ukei Y, Morota K, Kashii N, Kawamura J, Yamamura T. High temperature proton NMR study of yttrium doped barium cerates. *Solid State Commun* 2004;**130**(1–2):73–7.
5. Wu J, Li LP, Espinosa WTP, Haile SM. Defect chemistry and transport properties of $Ba_xCe_{0.85}M_{0.15}O_{3-\delta}$. *J Mater Res* 2004;**19**(8):2366–76.
6. Osman N, Talib IA, Hamid HA, Jani AM. Characterization, electrical conduction and stability of Yb-doped barium cerate prepared by sol–gel method. *Ionics* 2008;**14**(5):407–13.
7. Park ET, Goretta KC, de Arellano-López AR, Guan J, Balachandran U, Dorris SE, et al. High-temperature deformation of $BaCe_{1-x}Y_xO_{3-y}$ ($0.05 \leq x \leq 0.2$). *Solid State Ionics* 1999;**117**(3–4):323–30.
8. López-Robledo MJ, Vaquero-Aguilar C, Martínez-Fernández J, Peña JI, Sayir A, Jiménez-Melendo M. Processing and mechanical behavior at elevated temperatures of directionally solidified proton conducting perovskites. *J Eur Ceram Soc* 2010:022, doi:10.1016/j.jeurceramsoc.2010.05.
9. Vaquero-Aguilar C, López-Robledo MJ, Martínez-Fernández J, Real C, Jiménez-Melendo M. High-temperature mechanical behavior of polycrystalline yttrium-doped barium cerate perovskite. *J Eur Ceram Soc* 2010, doi:10.1016/j.jeurceramsoc.2010.05.023.
10. Wu J, Davies RA, Islam MS, Haile SM. Atomistic study of doped $BaCeO_3$: dopant site-selectivity and cation nonstoichiometry. *Chem Mater* 2005;**17**(4):846–51.
11. Wu J, Webb SM, Brennan S, Haile SM. Dopant site selectivity in $BaCe_{0.85}M_{0.15}O_{3-\delta}$ by extended X-ray absorption fine structure. *J Appl Phys* 2005;**97**(5):1–7, 054101.
12. Mather GC, Islam MS. Defect and dopant properties of the $SrCeO_3$-based proton conductor. *Chem Mater* 2005;**17**(7):1736–44.
13. Shannon RD. Revised effective ionic radii and systematic studies of interatomic distances in halides and chalcogenides. *Acta Cryst* 1976;**A32**:751–67.
14. Knight KS, Bonanos N. The crystal structure of some doped and undoped alkaline earth cerate perovskites. *Mater Res Bull* 1995;**30**(3):347–56.
15. Knight KS, Bonanos N. Space group and lattice constants for barium cerate and minor corrections to the crystal structures of $BaCe_{0.9}Y_{0.1}O_{2.95}$ and $BaCe_{0.9}Gd_{0.1}O_{2.95}$. *J Mater Chem* 1994;**4**(6):899–901.
16. Knight KS. Oxygen vacancy ordering in neodymium-doped barium cerate. *Solid State Commun* 1999;**112**:73–8.
17. Bravo-León A, Jiménez-Melendo M, Domínguez-Rodríguez A. Mechanical and microstructural aspects of the high temperature plastic deformation of yttria-stabilized zirconia polycrystals. *Acta Metal Mater* 1992;**40**(10):2717–26.
18. Flacher O, Blandin JJ, Plucknett KP. Effects of zirconia additions on the superplasticity of alumina–zirconia composites. *Mater Sci Eng A* 1996;**221**(1–2):102–12.
19. Jiménez-Melendo M, Domínguez-Rodríguez A, Bravo-León A. Superplastic flow of fine-grained yttria-stabilized zirconia polycrystals: constitutive equation and deformation mechanisms. *J Am Ceram Soc* 1998;**81**(11):2761–76.
20. Morita K, Kim B-N, Hiraga K, Sakka Y. Yield drop in high-strain-rate superplastic deformation of ZrO_2–30 vol% $MgAl_2O_4$ spinel composite. *Phil Mag Lett* 2003;**83**(9):533–41.
21. Dokko PC, Pask JA. High-temperature stress–strain behavior of MgO in compression. *J Am Ceram Soc* 1979;**62**(9–10):433–9.
22. Mazdiyasni KS, Lipsitt HA. Mechanical properties of polycrystalline TiC. *J Am Ceram Soc* 1982;**65**(2):104–10.
23. Sakai T, Jonas JJ. Dynamic recrystallization: mechanical and microstructural considerations. *Acta Metall* 1984;**32**(2):189–209.
24. McQueen HJ, Ryan ND. Constitutive analysis in hot working. *Mater Sci Eng A* 2002;**322**(1–2):43–63.
25. Lin YC, Chen M-S, Zhong J. Prediction of 42CrMo steel flow stress at high temperature and strain rate. *Mech Res Commun* 2008;**35**:142–50.
26. Liu J, Cui Z, Li C. Modelling of flow stress characterizing dynamic recrystallization for magnesium alloy AZ31B. *Comp Mater Sci* 2008;**41**(3):375–82.
27. Nieh TG, Wadsworth J, Sherby OD. *Superplasticity in metals and ceramics*. Cambridge: Cambridge University Press; 1997.
28. Glöckner R, Islam MS, Norby T. Protons and other defects in $BaCeO_3$: a computational study. *Solid State Ionics* 1999;**122**(1–4):145–56.